Effect of pre-heating and post-weld heat treatment on structure and mechanical properties of laser beam-welded Ti₂AlNb-based joints

Dmitrii Panov [a], [*], Stanislav Naumov [a], Nikita Stepanov [a], Vitaliy Sokolovsky [a], Elena Volokitina [a], Nikolai Kashaev [b], Volker Ventzke [b], René Dinse [b], Stefan Riekehr [b], Elizaveta Povolyaeva [a], Nadezda Nochovnaya [c], Evgeniy Alekseev [c], Sergey Zherebtsov [a], Gennady Salishchev [a]

[a] *Laboratory of Bulk Nanostructured Materials, Belgorod State University, 85 Pobeda Str., 308015, Belgorod, Russian Federation*
[b] *Institute of Materials Mechanics, Department of Laser Processing and Structural Assessment, Helmholtz-Zentrum Hereon, Max-Planck-Str. 1, D-21502 Geesthacht, Germany*
[c] *Federal State Unitary Enterprise "All-Russian Scientific Research Institute of Aviation Materials", 17 Radio Str., 105005, Moscow, Russian Federation*

ARTICLE INFO

ABSTRACT

The effect of pre-heating and post-weld heat treatment on microstructure and mechanical properties of laser-welded joints in a Ti–23Al–23Nb-1.4V-0.8Zr-0.4Mo-0.4Si (at.%) alloy was studied. Laser beam-welding was carried out at room temperature as well as after pre-heating up to 800°C. The post-weld heat treatment comprised either air quenching from 920°C followed by aging at 800°C or only aging at 800°C. The microstructure of the fusion zone consisted of columnar β-grains after welding at room temperature and 400 °C or both the columnar and large equiaxed crystals at 600 and 800 °C. An increase in the pre-heating temperature caused the columnar β-crystals growth as well as an increase in the fusion zone and heat-affected zone widths. Meanwhile, a decrease in the Al and Ti content, as well as an increase in both the porosity and gaseous elements content (O and N) after welding at 600–800 °C were found. The microhardness of each joint obtained after welding with pre-heating temperatures up to 600 °C was lower than that of the base material. All the welded joints showed the yield strength and ultimate tensile strength levels between 1070 and 1110 MPa, which correspond to approximately 80% of the base metal level. Reasonable total elongation of the joint was achieved after welding at 400 °C (4.3%). The post-weld heat treatment involving air quenching from 920 °C with subsequent aging at 800 °C for 6 h demonstrated the best results. The heat treatment resulted in the precipitation of the O- and α₂-phases and an increase in total elongation to 6.5%.

1. Introduction

Orthorhombic titanium aluminide (Ti₂AlNb) based alloys are very attractive high-temperature materials for gas turbine and automotive engine components due to their high specific strength, low density, high oxidation resistance, and good creep resistance [1,2]. Replacing nickel-based superalloys with orthorhombic titanium aluminides can reduce the weight of some turbine parts. At the same time, Ti₂AlNb-based alloys have significantly higher ductility and toughness in comparison with γ-TiAl- and α₂-Ti₃Al based alloys. Meanwhile, in some cases Ti₂AlNb, like any structural alloy, must be welded to fabricate parts with complex geometries. However, poor weldability of the Ti₂AlNb based alloys is one of the most significant aspects that limits their wider application [2].

Several studies have examined welding of Ti₂AlNb-based alloys using different methods: brazing [3], diffusion welding [4], gas tungsten arc [5], resistance spot-welding [6], electron beam-welding [7], friction stir-welding [8] and laser beam-welding (LBW) [9]. LBW can be considered as one of the most promising techniques for obtaining joints of Ti₂AlNb-based alloys because of high process efficiency, the possibility of both automatization [10], and manufacturing of complex structures without additional mechanical treatment [11].

Despite the above-mentioned advantages, the formation of a coarse columnar structure of the β-phase in the fusion zone can result in a decrease in strength and ductility of laser-welded Ti₂AlNb joints [12]. In addition, the possible introduction of gases in the weld zone and the formation of microcracks and pores also contribute to a decrease in the mechanical properties [13,14]. Since the β-phase is metastable and

undergoes the β→O and/or β→α_2 transformations at high temperatures [15], post-weld heat treatment (PWHT) can stabilize the structure and properties of the joints [10]. PWHT usually consists of quenching from the β phase field [16] and aging at temperatures in the range of 800–840 °C, resulting in the O-phase precipitation [17].

In addition, due to insufficient ductility of the Ti_2AlNb-based alloys, the formation of transverse cracks in the joints at high cooling rates (more than 300 K/s [18]) is possible. Cracking can be suppressed by pre-heating above the brittle-to-ductile transition temperature to reduce the cooling rate after welding [19]. For instance, pre-heating brittle intermetallic alloys to 600 °C and above eliminates the welding crack formation in the weld zone [20]. Hence, high-quality laser-welded Ti_2AlNb joints might be obtained due to PWHT [21].

Although several studies focused on the optimization of welding and PWHT parameters and examination of the structure-properties relations in the obtained joints, there is no systematic information on the effect of pre-heating and PWHT on different aspects of LBW joints of Ti_2AlNb-based alloys. The present work aims to fill this gap and to (i) obtain a better understanding of the processing condition-structure-properties relationships in LBW of Ti_2AlNb-based joints and (ii) establish optimal LBW and PWHT conditions for such alloys.

2. Experimental details

An ingot of a Ti–23Al–23Nb-1.4V-0.8Zr-0.4Mo-0.4Si (at.%) alloy was produced by triple remelting using a vacuum arc skull furnace. The following phase fields were found in the program alloy in earlier investigations depending on temperature: O < 770 °C < β+O < 900 °C < α_2+β+O < 1000 °C < α_2+β < 1050 °C < β [22]. Therefore, the thermomechanical processing of the ingot comprised: pre-heating to 1180 °C and soaking for 2 h → compression along the main axis with a strain of 30% (1st step in Fig. 1) → cooling to 1130 °C → multiaxial forging with changing the loading direction by 90° each next step (2nd and 3rd step in Fig. 1) and drawing with cooling to 980 °C (4th step in Fig. 1). After the drawing, the workpiece was cooled to 950°C and compressed with a strain of 70–75% (Fig. 1). The condition after compression was used as the initial one in this study.

Then plates measured 2 × 15 × 22 mm³ were cut parallel to the last compression direction using a wire electrical-discharge machining (EDM) Sodick VL400Q. LBW of the obtained plates was carried out at room temperature or with pre-heating temperatures of 400 °C, 600 °C and 800 °C. A ytterbium fiber laser YLS-8000 with a maximum power of 8.0 kW and a chamber with a controlled protective gas atmosphere (Ar of 99.998% purity) was used to conduct autogenous butt welding. Ceramic heaters were used for pre-heating and the heat transfer to the specimens was ensured by using ceramic plates with high heat conduction. The pre-heating temperature was controlled with a thermocouple (type N, TC Direct) connected to the ceramic heaters. The following LBW process parameters, identified based on our previous studies, were applied: laser power 4.0 kW, welding speed 3.0 m/min, laser defocusing distance 0.0 mm [23].

PWHT was performed using a Nabertherm LT 5/12/P320 furnace.

Two different PWHT modes were used: PWHT1 – the samples were heated to 920°C, held for 2 h with subsequent air cooling to ambient temperature, and, then, subjected to aging at 800°C for 6 h, followed by air cooling; PWHT2 – the samples were subjected to aging at 800°C for 6 h, followed by air cooling. To prevent oxidation, the specimens were sealed in a ceramic capsule with protective argon gas and titanium chips.

The microstructure of the joints was investigated by transmission electron microscopy (TEM) and scanning electron microscopy (SEM). TEM observations were performed using a JEOL JEM-2100 transmission electron microscope at an accelerating voltage of 200 kV. For TEM observations, templets with a thickness of 300 μm were cut using EDM and thinned to 100 μm on a LaboPol-5 mechanical grinding-polishing machine. Further, disks with a diameter of 3 mm cut from the thinned plates, were subjected to double-jet electrolytic polishing and perforation using Struers Tenupol-5 with an electrolyte comprising of 60 ml of $HClO_4$, 600 ml of CH_3OH and 360 ml C_4H_9OH at 27 V and −30 °C. After perforation, the foils were washed in distilled water and ethyl alcohol and thoroughly dried.

SEM-observations were carried out using a Nova NanoSEM 450 and FEI ESEM Quanta 200 electron microscopes equipped with an EDAX Hikari EBSD camera, a back-scattered electron (BSE), and energy-dispersive X-ray spectroscopy (EDS) detectors, at an accelerating voltage of 30 kV. The sample surface for microstructural studies was ground with abrasive papers. Then the surface was polished with OP-S NonDry suspension using Struers MD Chem equipment. The final cleaning of the surface was carried out using an ultrasonic bath Sapphire in acetone for 30 min, followed by cleaning with Fischione Plasma Cleaner. Phases and structural geometric characteristics were identified using TSL OIM analysis, from which the points with the confidence index (CI) < 0.1 were excluded. The Nb content in gas pore walls was estimated on fracture surfaces using the EDS-detector.

X-ray phase analysis was performed by a Rigaku SmartLab X-ray diffractometer using CuK_α radiation. The study was carried out in the range of 2θ angles 15–120° with a step of 0.02°.

The content of oxygen and nitrogen was examined using a METEK-300/METEK-600 analyzer with Meta Terminal software. Probes of the fusion zone with a weight of ~4 g were cut using EDM. Then the surface was ground and cleaned within the ultrasonic bath in acetone for 30 min.

Tensile testing was performed using an Instron 5882 machine at room temperature and an initial strain rate of 10^{-3} s^{-1}. Tensile specimens cut by EDM were mechanically ground and polished as per the above-mentioned procedure. The loading direction was perpendicular to the welding line. The geometry of the tensile specimens with the gauge measured 6 × 3 × 1.5 mm³ is presented in Fig. 2a. At least two specimens were examined per each condition. Additionally, the local strain distribution along the gauge was measured. For that purpose, transverse lines at a distance of 1 mm were drawn at each specimen. The spacing between the lines was measured before and after testing using an Olympus STM6 measuring microscope. Microhardness testing was performed across the as-received joints using a Vickers 402MVD
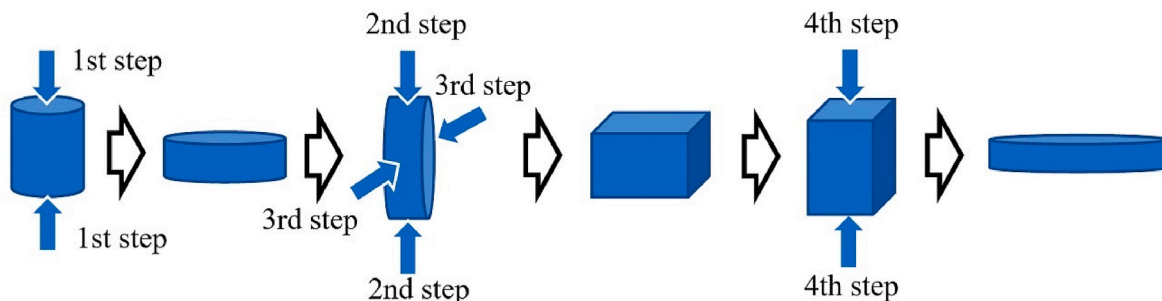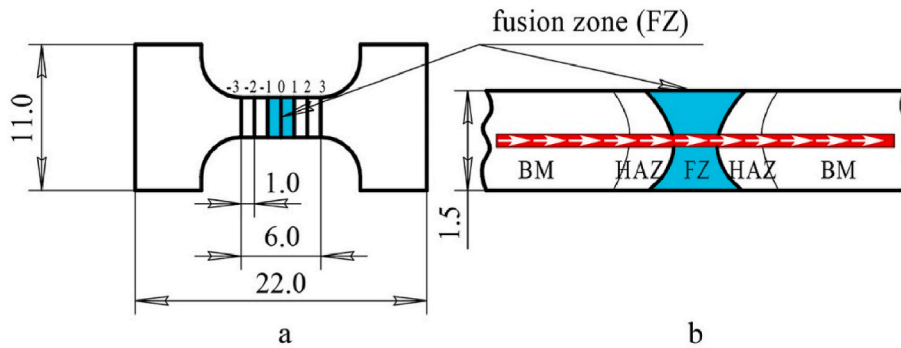

Fig. 1. Scheme of deformation path.

Fig. 2. (*a*) Tensile specimen geometry and (*b*) scheme of microhardness testing. In Fig. 2b, the red line and white arrows indicate the location and direction of microhardness testing, respectively. All of the dimensions are in mm.

microhardness tester with a step of 0.1 mm, a load of 0.2 kg, and a dwell time of 15 s ($HV_{0.2}$) (Fig. 2b).

3. Results and discussion

3.1. Initial structure

The initial structure of the program alloy is shown in Fig. 3. The following phases were detected by XRD (Fig. 3a): β- (an ordered B2 phase with the Pm3m symmetry), O- (an ordered orthorhombic phase with the Cmcm symmetry), and α_2-phases (an ordered DO_{19} phase with the $P6_3/mmc$ symmetry). The β-phase matrix, globular α_2-phase, and lamellar O-phase particles were also observed in SEM-BSE images (Fig. 3b and c). The content of Nb (the element with the highest atomic number in the alloy) gradually decreased from the maximum in β- to O-, and then to the α_2-phase, due to which these phases are visible as bright, gray, and dark areas in the BSE images, respectively [24]. The structure comprised of large elongated primary β-phase grains with a length of 410 ± 50 μm and a width of 85 ± 20 μm (Fig. 3b). The primary β-grains in turn are composed of smaller grains/subgrains with a diameter of 3.1 ± 1.3 μm (Fig. 3c). Globular particles of the α_2-phase with a diameter of 1.2 ± 0.7 μm are found along the β-grain/subgrain boundaries. Lamellae of the O-phase with a length of 200 ± 60 nm and a width of 30 ± 10 nm

exist within the β-grains/subgrains (Fig. 3d). The phase composition (as per TEM data), included 34% of the α_2-phase, 26% of the β-phase, and 40% of the O-phase.

3.2. Weld seam appearance

The welds produced by LBW with different pre-heating temperatures are shown in Fig. 4. After LBW at RT transverse cracks with a length of 0.5 ± 0.1 mm were found (Fig. 4a). The hot crack formation was likely associated with high internal welding stresses. Pre-heating to 400 °C and above decreased the crack formation probability. LBW in the keyhole mode resulted in the formation of more pronounced underfills, which are caused by the expulsion of the welded material. The appearance is typical for LBW of Ti-alloys at high welding speeds combined with high laser power levels in a keyhole mode [25]. The welds obtained at RT and 400 °C had a bright silvery weld bead and seam root (Fig. 4a and b) that indicated an absence of oxidation [26]. Upon pre-heating to 600 °C, the weld exhibited a yellowish tint (Fig. 4c) that is considered acceptable for welded joints [27]. However, the purple color of the welds after welding with pre-heating to 800 °C indicated severe oxidation (Fig. 4d). The Ti_2AlNb-based alloys are prone to corrosion at temperatures above 700 °C, therefore the evidence of active oxidation at 800 °C is not surprising [28].
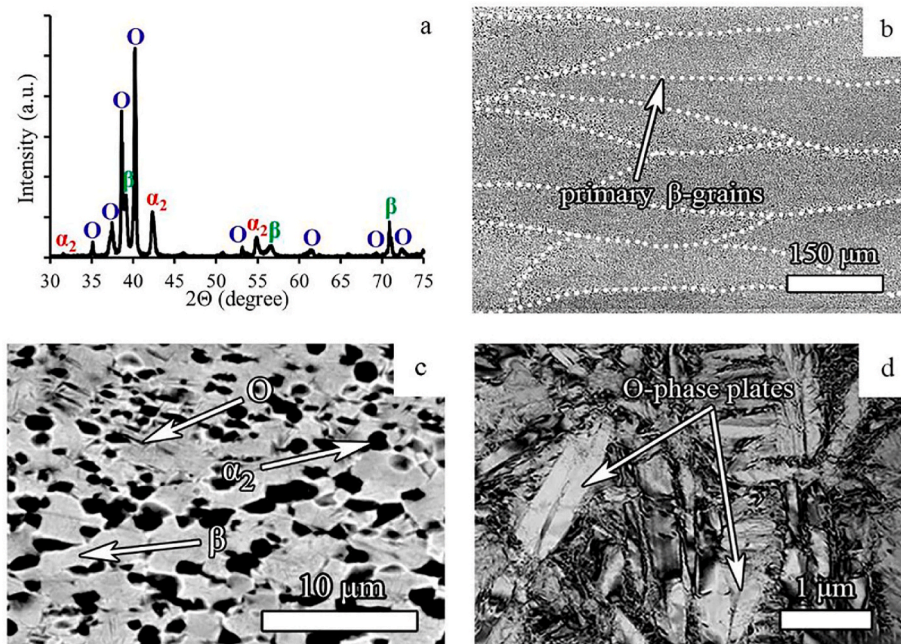

Fig. 3. Microstructure of the program alloy in the initial condition: (*a*) XRD pattern, (b), (c) BSE-SEM, and (*d*) bright field TEM images.
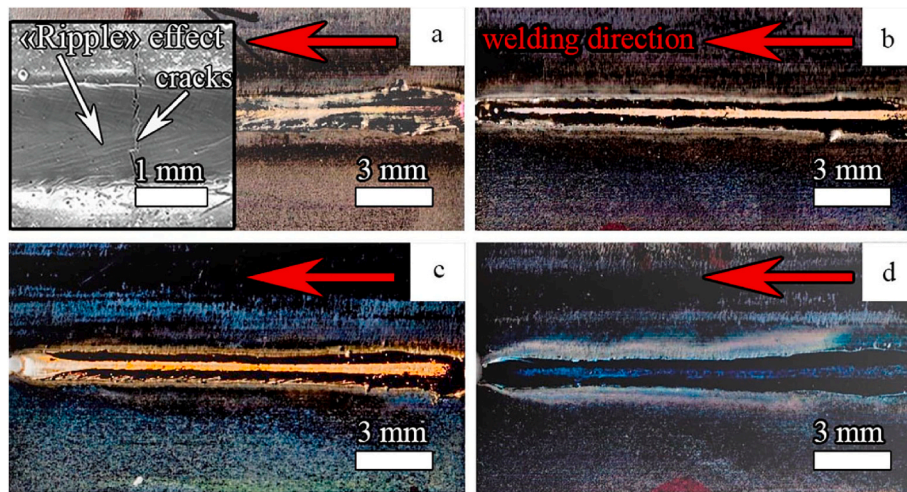
Fig. 4. Appearance of welds obtained at (*a*) RT, (*b*) 400°C, (*c*) 600°C, and (*d*) 800°C. Insert in 4a is BSE-SEM image. Red arrows indicate the laser beam motion direction.

3.3. Weld seam microstructure

Structure of the transverse section of the joints after LBW at different pre-heating temperatures is shown in Figs. 5 and 6. Three zones can be clearly distinguished in the welded joint (Fig. 5): the fusion zone (FZ), the heat-affected zone (HAZ), and the base metal (BM). According to Liu et al. [29] and Wang et al. [27], the FZ possessed the hourglass-shaped cross-section due to more significant melting (less efficient heat dissipation) in the upper and lower part compared to the middle part. FZ predominantly consisted of the β-phase. The cooling rate was high enough to retain the β-phase structure in FZ and mostly suppress the O- and α_2-phases formation during solidification of the melted material that can also be associated with the effect of a high Nb content [21]. However, at 800 °C, less than 10% of the O-phase lamellae were detected within FZ (Supplementary Materials, Fig. S1).

Depending on the phase composition, HAZ can be divided into the following zones: HAZ1 - β (Fig. 5c), HAZ2 - β + α_2 (Fig. 5d), HAZ3 - β + α_2 + O (Fig. 5e). A similar structure of HAZ in Ti$_2$AlNb-based alloys was also reported by Wang et al. [27] and Zhang et al. [21]. In HAZ1, large β-phase grains were observed (Fig. 5c). Meanwhile, the α_2-and O-phases were completely dissolved upon heating during welding; subsequent fast cooling almost completely suppressed their precipitation. In HAZ2 the globular α_2-phase was partially preserved (Fig. 5d) because the heating temperatures were not sufficient to the complete $\alpha_2 \rightarrow \beta$ transformation [21]. In comparison to BM, HAZ3 consisted of β + O + α_2 (Fig. 5e) where the O-phase partially transformed into the β-phase upon heating, while the α_2-phase was mainly retained. For all the considered pre-heating temperatures, the HAZ structure was qualitatively similar. It should be
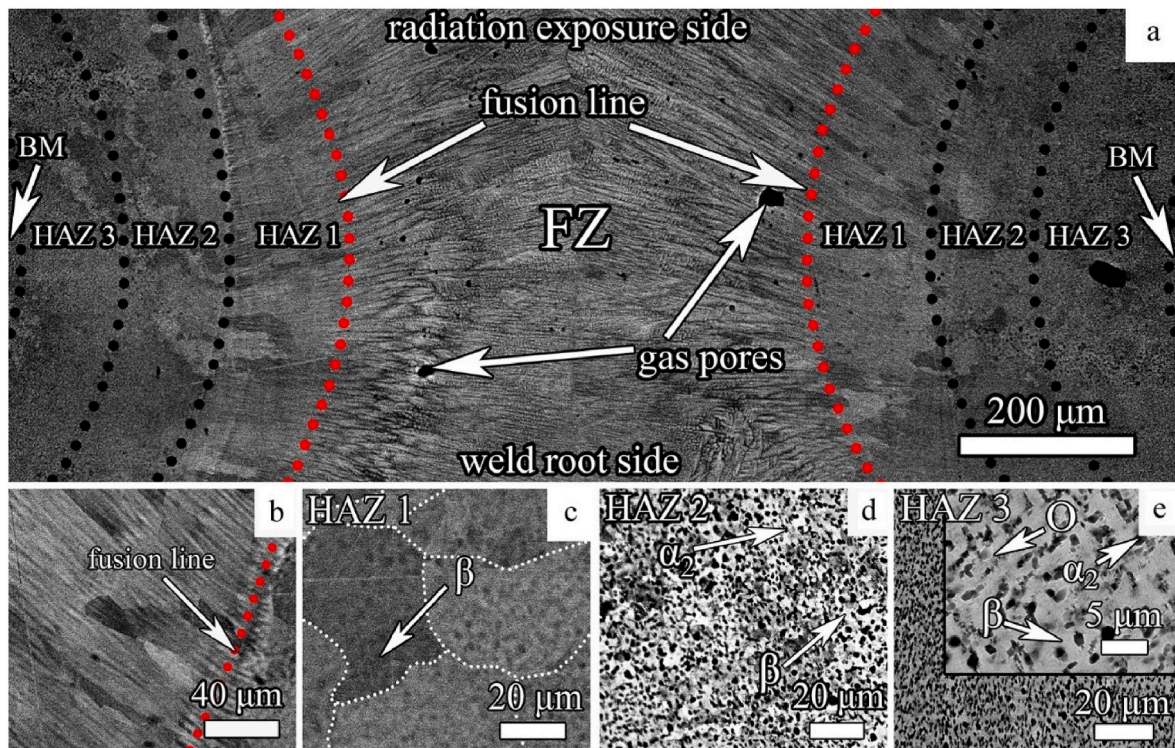

Fig. 5. Transverse structure of (*a*) the weld seam, (*b*) FZ, (*c*) HAZ1, (*d*) HAZ2, and (*e*) HAZ3 after LBW at RT.
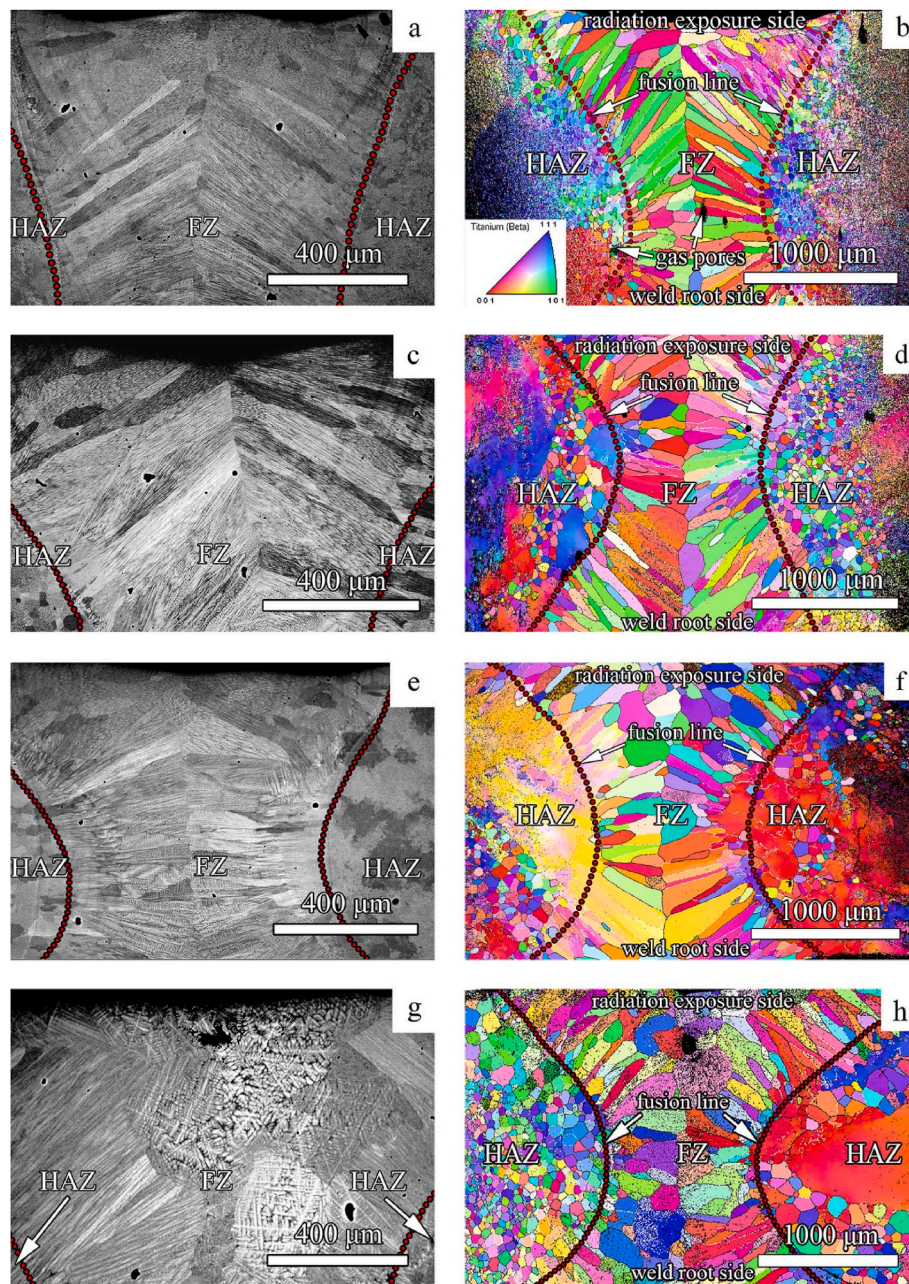
Fig. 6. Transverse sections of the weld zones after LBW at (a, b) RT, (c, d) 400°C, (e, f) 600°C, and (g, h) 800°C; SEM BSE image and EBSD IPF map shown respectively in the left and right parts of an image. Black and white lines denoted boundaries with low- (3–15°) or high-angle (>15°) misorientations, respectively.

noted that the weld line was perpendicular to the elongated, primary β-grains (Supplementary Materials, Fig. S2).

EBSD IPF maps (Fig. 6) show the effect of pre-heating temperature on grain structure of FZ. The fusion zone after LBW at temperatures from RT to 400°C consisted of elongated β-grains/subgrains with an average length of 300–350 μm aligned from the fusion line (FL) to the center of FZ (Fig. 6a–f). An increase in the pre-heating temperature from RT to 800°C resulted in a gradual increase in width of the elongated grains/subgrains from ~55 to ~125 μm, respectively, due to decreased heat removal and lower crystallization rates. However, at 600 and 800 °C, large globular grains with a diameter of ~300 μm were found in the middle of FZ. After preheating to 800 °C, large globular grains occupied a large portion of the FZ. So, an increase in the pre-heating temperature from RT to 800 °C caused some growth of the β-grain area from 0.007 ± 0.001 mm^2 to 0.012 ± 0.001 mm^2, respectively (Fig. 7a). Meanwhile, only a slight increase in the FZ width with increasing the pre-heating

temperature from RT to 800 °C was also revealed.

An increase in the pre-heating temperature increased the size of β-grains in the HAZ1. For instance, after LBW at 800 °C, some β-grains enlarged to 1 mm (Fig. 6h), while, at RT, the size of β-grains in the HAZ1 did not exceed 70 μm (Fig. 6b). This difference can be associated with (i) dissolution of the α$_2$-particles (Fig. 5c) pinned boundaries of the β-grains and thereby preventing grain growth and (ii) a general increase in temperatures with rising of the pre-heating temperature. Besides, an increase in the pre-heating temperature resulted also in widening the HAZ1 as well as the HAZ (Fig. 7a).

Globular grain structure was detected near the FZ/HAZ boundary, i. e. FL (Figs. 5a and 6), and in some parts of the HAZ. An increase in the pre-heating temperature from RT to 800 °C resulted in an increase in the average β-grain/subgrain size along FL from ~40 to ~110 μm, respectively. It should be noted that FL is a possible site of failure [30] due to a coarse structure, the presence of pores, and rather high local stresses. So,
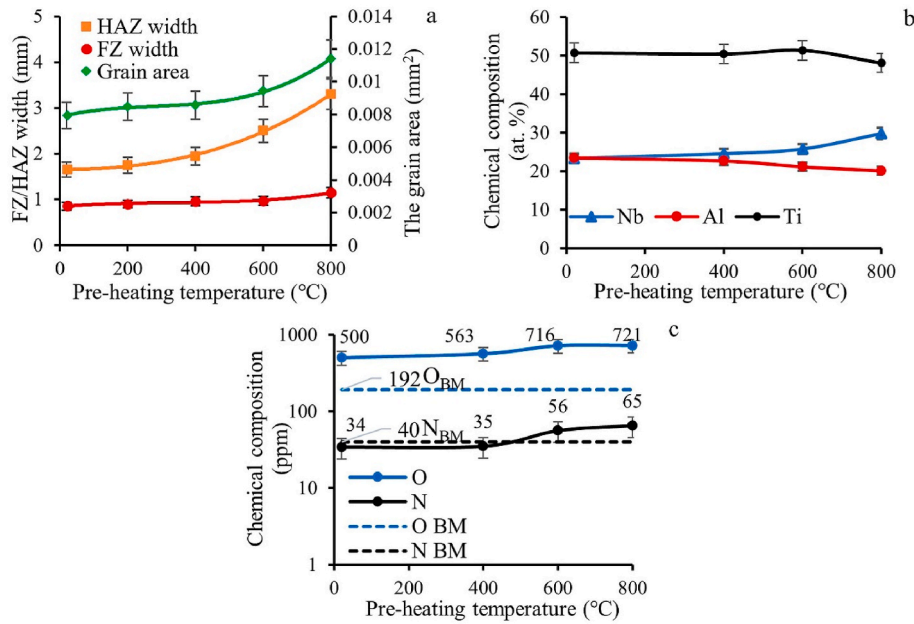
Fig. 7. (a) Geometric parameters and (b)–(c) composition of welds as a function of pre-heating temperature. O_{BM} and N_{BM} – the oxygen and nitrogen content in the base metal.

doubling of the β-grain/subgrain size nearby FL can result in loss in ductility. The width of the HAZ increased pronouncedly from 1.6 to 3.3 mm with increasing the pre-heating temperature due to increased heat input.

It should be noted that internal uniformly distributed spherical pores were found within FZ (Figs. 5 and 6). The size of the pores slightly grew with increasing the pre-heating temperature from ~40 μm at room temperature to the maximum size of ~50 μm after LBW at 800 °C. According to Zhan et al. [31], the porosity of LBWed joints of TA15 titanium alloy can be caused by water absorption and Al evaporation. Apparently, an increase in the gas pores size was associated with increasing the pre-heating temperature which intensified the hydrogen accumulation and Al evaporation process [31]. These processes occurred during LBW because of very high laser power-density input

[27]. At the same time, fast solidification of a molten pool caused the capture of hydrogen and Al vapor bubbles. A corresponding decrease in the content of Al in FZ after LBW at 600–800 °C was indeed detected in FZ (Fig. 7b). A similar effect was also observed after selective laser melting of a Ti$_2$AlNb-based intermetallic alloy [32]. A decrease in the Ti content (most likely due to evaporation of Ti) was also obtained at 800 °C (Fig. 7b). Meanwhile, the Nb content in gas pore walls with an increase in the pre-heating temperature from 400 to 800°C increased dramatically from 47 to 66%. Furthermore, LBW at 800 °C resulted in a decrease in the Ti and Al contents to 9% and 21%, respectively. It is important to note that the content of oxygen and nitrogen gradually increased with pre-heating temperature (Fig. 7c). Dary and Pollock [33] and Yan et al. [34] found that an increase in the content of oxygen can result in decreasing ductility.
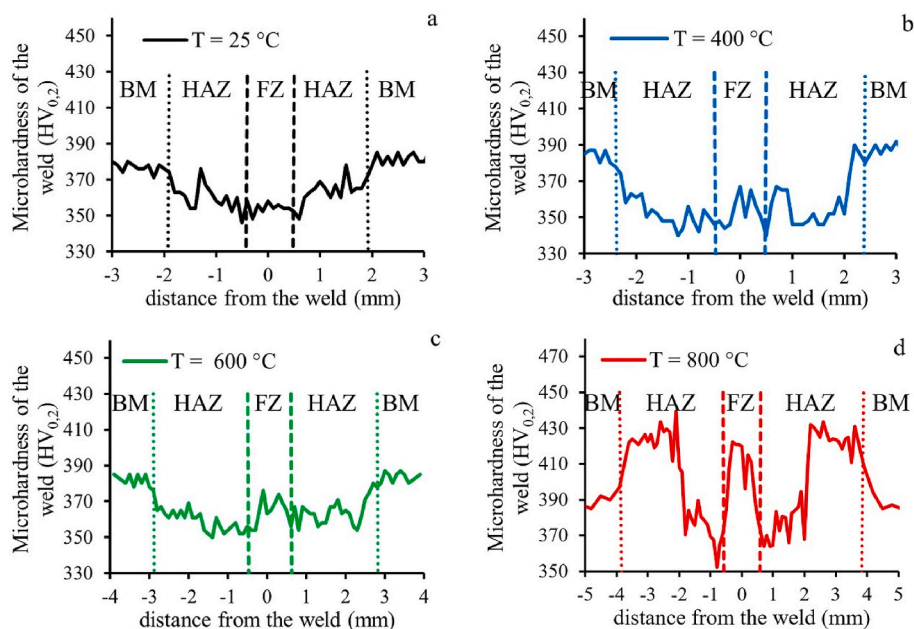

Fig. 8. Microhardness distribution of the joints after LBW at (a) RT, (b) 400 °C, (c) 600 °C, and (d) 800 °C.

3.4. Mechanical properties and deformation behavior of the joints

The microhardness distribution across the weld is shown in Fig. 8. At RT and 400–600 °C, the microhardness of the welded seams slightly decreased to 340–375 $HV_{0.2}$, while the BM hardness was 360–390 $HV_{0.2}$. For Ti_2AlNb-based alloys, the main hardening mechanism is precipitation hardening by the O-phase particles [8], therefore the dissolution of the O-phase in FZ resulted in a decrease in microhardness in comparison with BM. Meanwhile, the volatility of hardness was very high at 800 °C (Fig. 8d). For example, three conspicuous peaks in the middle part of FZ and HAZ were observed. An increase in microhardness of FZ can be associated with enrichment with oxygen and nitrogen (Fig. 7c) that caused significant strengthening [35]. At the same time, fine needle-like particles of the O-phase arisen within large β-phase grains (Supplementary Materials. Fig. S1b) due to slower cooling rates during LBW contributed to precipitation strengthening of FZ and HAZ (HAZ2 and HAZ3 in particular). It is worth noting that similar (yet less visible) effects were observed after welding at 600 °C (Fig. 8c).

It should be mentioned that the scatter of the welded joint's hardness should not exceed 20% to avoid a drop in mechanical properties [36]. However, the relative hardness change after LBW at various temperatures did not exceed 11%.

Tensile stress-strain curves and mechanical properties of the program alloy in the initial condition and after LBW are shown in Fig. 9. The alloy in the initial condition exhibited high strength (yield strength YS = 1320 MPa, ultimate tensile strength UTS = 1390 MPa) together with a reasonable both strain hardening capacity and total elongation (TE = 11.3%). After welding, both strength and ductility deteriorated. Welding conditions had a very limited effect on strength - the yield strength and ultimate tensile strength of the joints were within narrow ranges of 1070–1100 MPa and 1080–1110 MPa, respectively. The ratio between the ultimate tensile strength of the initial material and the joints was ~0.8. Meanwhile, ductility of the joints showed a strong dependence on the pre-heating temperature. The joint after LBW at 400 °C demonstrated the best total elongation (4.3%). Stress-strain curves for the joints, obtained at RT, 600 °C, and 800 °C showed only limited plastic strain thus the corresponding values of TE were below 2%.

The results of local strain measurements along the gauge length are shown in Fig. 10a. The local strain values correlated well with TE, obtained during tensile tests (Fig. 9). Significant heterogeneity of strain distribution was revealed. The maximum strain values corresponded to the center of the specimens, i.e. to FZ and HAZ. Note that microhardness measurements have revealed decreased microhardness in these areas (Fig. 8). At FZ/HAZ region, the maximum of local strain reached ~12% at 400 °C, ~6% at RT, and <2% at 600–800 °C.

To get more insights into the deformation behavior of the welds, the surface relief of different parts of gauges was examined. After welding at 400 °C, straight sharp lines indicated the development of slip in two different directions in the center of the specimen, i.e. in FZ with the single β-phase structure (Fig. 10b). Similar slip patterns were found in HAZ located ~1.5 mm away from the center of the specimen (Fig. 10c),

despite significantly lower local strain in this area and the presence of the α_2 and O particles. No signs of slip were detected in BM, which correlated well with low values of local strain in this area (Fig. 10d). Somewhat different surface relief was observed after LBW at 600 °C. In the central (FZ) part, well-developed slip patterns were found (Fig. 10e). Yet, the slip lines were curved and indicated activation of only one slip system. Lower slip intensity was detected in HAZ (Fig. 10f). Meanwhile, no-slip patterns were found in BM (Fig. 10g). After LBW at 800 °C, any surface relief along the gauge length was not detected.

SE - SEM images of the fracture surfaces after tensile tests are shown in Fig. 11. Fracture of all samples occurred through FZ perpendicularly to the loading direction. SEM-overviews of the fracture surfaces obtained at RT and 400 °C revealed only a few small pores (Fig. 11a and b). At 600 and 800 °C, both large and small pores were observed (Fig. 11c and d). Secondary cracking was observed in the fracture surfaces of all specimens (Fig. 11e–h). The average length of the secondary cracks increased with an increase in the pre-heating temperature from ~50 μm at RT and 400 °C (Fig. 11a and b) to ~500 μm at 600–800 °C (Fig. 11c). The crack formation was most likely associated with the transgranular cleavage fracture within the β-grain. The fracture mode found here is consistent with other results obtained for the welded joints of Ti alloys with a β structure [21].

Generally, plastic deformation of the joints after LBW with different pre-heating temperatures was located in FZ and HAZ (Fig. 10) due to both significantly higher strength of BM and a higher volume fraction of a soft β-phase in FZ (Fig. 8). Interestingly, the local ductility of FZ for pre-heating temperature of 400 °C (~12%) exceeded the total elongation of the base metal (11.5%). However, the ductility of the specimens welded at other temperatures was noticeably lower. We suggest the following factors were responsible for brittleness of the joints heated to 600 and 800 °C: (i) a coarse dendritic structure in FZ (Fig. 7a); (ii) a high percentage of nitrogen and oxygen (Fig. 7c); (iii) higher porosity in comparison with room temperature and 400 °C. According to the fracture surface examination (Fig. 11), the latter strongly affected ductility because single pores served as stress concentrators. On the other hand, the low ductility of the welds obtained at RT was most likely associated with the presence of hot cracks due to high residual stresses. The residual stresses were mostly released in the case of pre-heating to 400°C and above due to lower cooling gradients after welding. Thus, the preheating temperature of 400°C is suggested to be an optimal option for LBW of the program Ti_2AlNb-based alloy joints.

3.5. Post-weld heat treatment of the joints obtained at 400 °C

The previous results (Section 3.4) have demonstrated that the best mechanical characteristics, in particular ductility, were obtained after LBW with pre-heating at 400 °C. Therefore, in the present section, we focused on PWHT of these specimens. PWHT of the program alloy after LBW with other pre-heating temperatures was also performed, the obtained results are collected in Supplementary Materials (Figs. S3 and S4). PWHT modes included quenching from 920 °C and/or aging at
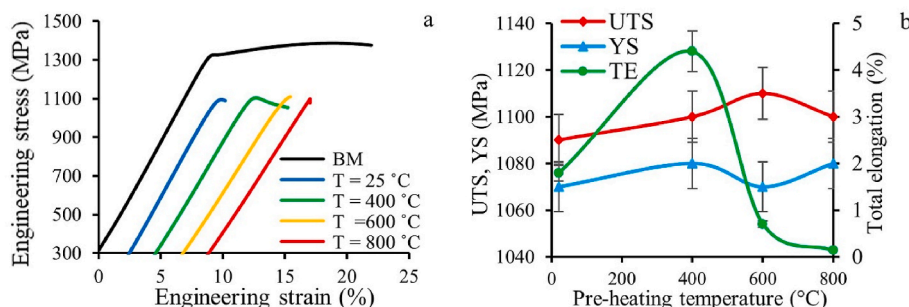

Fig. 9. (a) Stress-strain curves of the as-received condition and the joints and (b) dependence of mechanical properties on the pre-heating temperature.
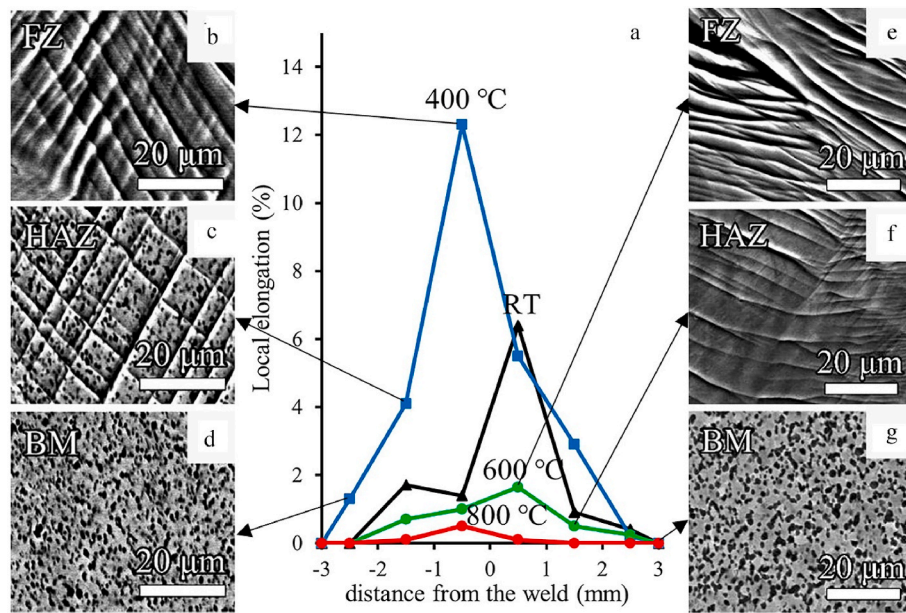
Fig. 10. (a) distribution of strain along the gauge length of the tensile specimens and gauge surface in the selected areas, illustrated by SEM-BSE images. BSE-micrographs demonstrated surface relief (*b*)–(*d*) for LBW 400 °C, (*e*)–(*g*) for LBW 600 °C.
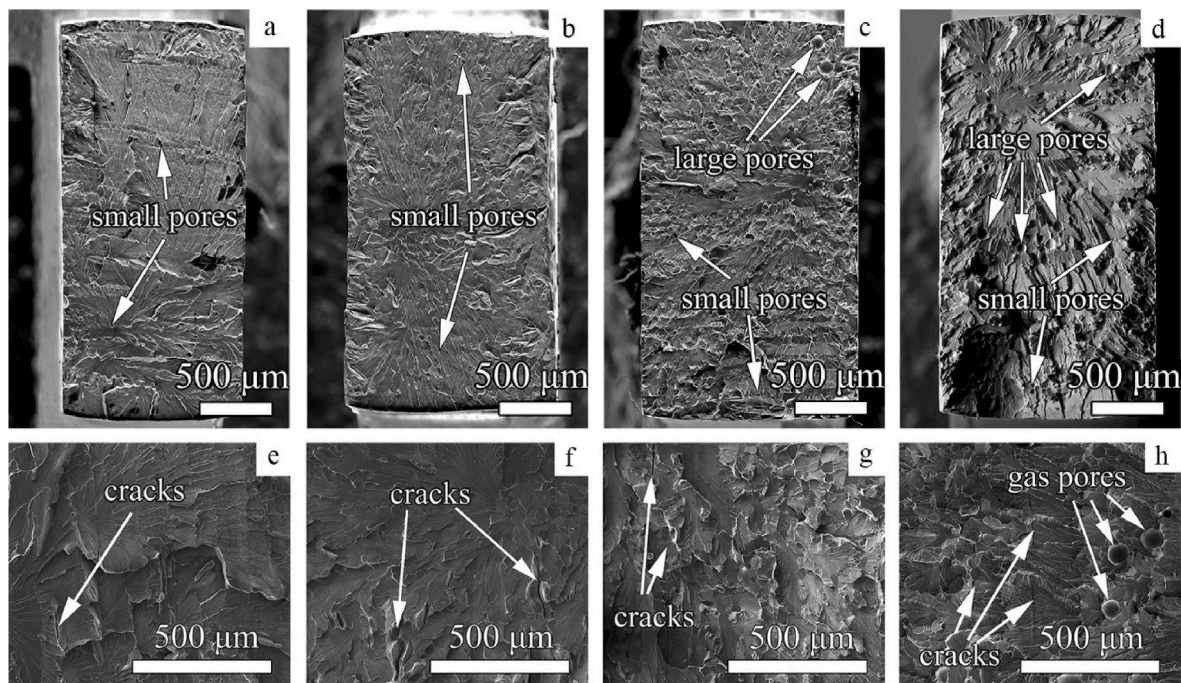

Fig. 11. SE - SEM photographs of the fracture surface of the tensile specimens after LBW at (*a*), (*e*) RT, (*b*), (*f*) 400°C, (*c*), (*g*) 600°C and (*d*), (*h*) 800°C.

800 °C that, according to Ref. [22], corresponded to the $\alpha_2 + \beta +$ O-phase and $\beta +$ O-phase fields, respectively.

The β-, O-, and α_2-phases were formed in the program alloy after both PWHT1 and PWHT2 (Fig. 12). After PWHT1, the O-lamellae with a length of $1.67 \pm 0.91\,\mu m$ and a width of $0.21 \pm 0.09\,\mu m$ and surrounded by the β-phase matrix were found in FZ (Fig. 13a and b). At the same time, a few α_2-particles most likely formed at 920 °C (i.e. in the $\alpha_2+\beta+$O-phase field) were detected along boundaries of the β-grains (Fig. 13a and c). After PWHT2, the O-lamellae had a length of $1.99 \pm 0.94\,\mu m$ and a width of $0.11 \pm 0.07\,\mu m$ (Fig. 13d). The volume fraction of the β-phase in FZ was 31% and 26% after PWHT1 and PWHT2, respectively.

The microhardness distribution across the weld was also examined

(Fig. 14). After PWHT1, a pronounced decrease in hardness in comparison with the as-welded condition (Fig. 8b) and low volatility of microhardness (320–340 HV) was observed (Fig. 14a). The microhardness values after PWHT2 were considerably higher (340–420 HV). In addition, a significant increase in hardness in FZ and adjacent areas of HAZ was detected (Fig. 14b).

Obviously, better mechanical properties were obtained after PWHT1 (UTS = 1140 MPa, YS = 1070 MPa, TE = 6.5%) compared to PWHT2 (UTS = 1190 MPa, YS = 1190 MPa, TE = 0.2%) (Fig. 15a). Strain localization in the samples after PWHT1 and PWHT2 was mainly observed within FZ/HAZ (Fig. 15b). Local ductility of other areas of the sample after PWHT2 was negligible, while after PWHT1 approximately
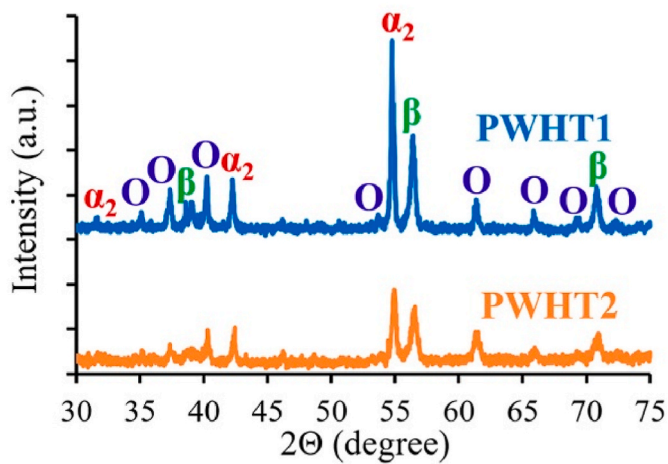
Fig. 12. XRD patterns of welds after LBW at 400 °C and subsequent heat treatment.

4–6% of strain was registered beyond FZ/HAZ.

Fracture surfaces after tensile tests were also examined (Fig. 15c and d). After PWHT1, ductile fracture occurred with the formation of dimples and quasi-brittle facets on the fracture surface (Fig. 15c). However, a mainly intercrystalline fracture was obtained after PWHT2 (Fig. 15d) that agrees with the results of earlier work [37]. Furthermore, several cracks were detected on the fracture surface. It should be noted that some gas pores were found in both cases.

The obtained results show a very promising combination of strength and ductility of the joints after, air quenching from 920 °C with subsequent aging at 800 °C (PWHT). On the one hand, high ductility (TE =

6.5%) might be associated with a high amount of the soft β-phase in the weld [1] in comparison with PWHT2. On the other hand, ductility can be associated with coarser O-phase precipitates. In contrast, the fine O-phase precipitates produced after soaking at 850 °C for 2 h, i.e. conditions similar to PWHT2, were earlier found to cause embrittlement [21]. In contrast to smooth hardness distribution after PWHT1, an increase in microhardness in FZ and adjacent HAZ after PWHT2 was also obtained (Fig. 14). Hence, additional strengthening of FZ after PWHT2 resulted in a loss of ductility. Also, it might be hypothesized that a high soaking temperature (920 °C) during PWHT1 can result in further release of residual stresses generated during welding thereby improving ductility.

4. Conclusions

The effect of pre-heating temperatures and post-weld heat treatments on the structure and mechanical properties of the laser-welded Ti–23Al–23Nb-1.4V-0.8Zr-0.4Mo-0.4Si (at.%) alloy was studied. The following results were obtained:

1. The most beneficial pre-heating temperature for laser beam welding (LBW) of Ti$_2$AlNb-based joints was 400 °C because of obtaining reasonable ductility (total elongation to fracture was 4.3%). At room temperature, hot cracks in the joints were formed. LBW at 600 and 800 °C was associated with the lack of ductility due to coarsening of dendritic structure in the fusion zone, enrichment of the fusion zone by nitrogen and oxygen concentration, and an increase in porosity. The yield strength and ultimate tensile strength of the LBWed joints were in the range of 1070–1110 MPa that corresponded to ~80% of the strength of the base metal.
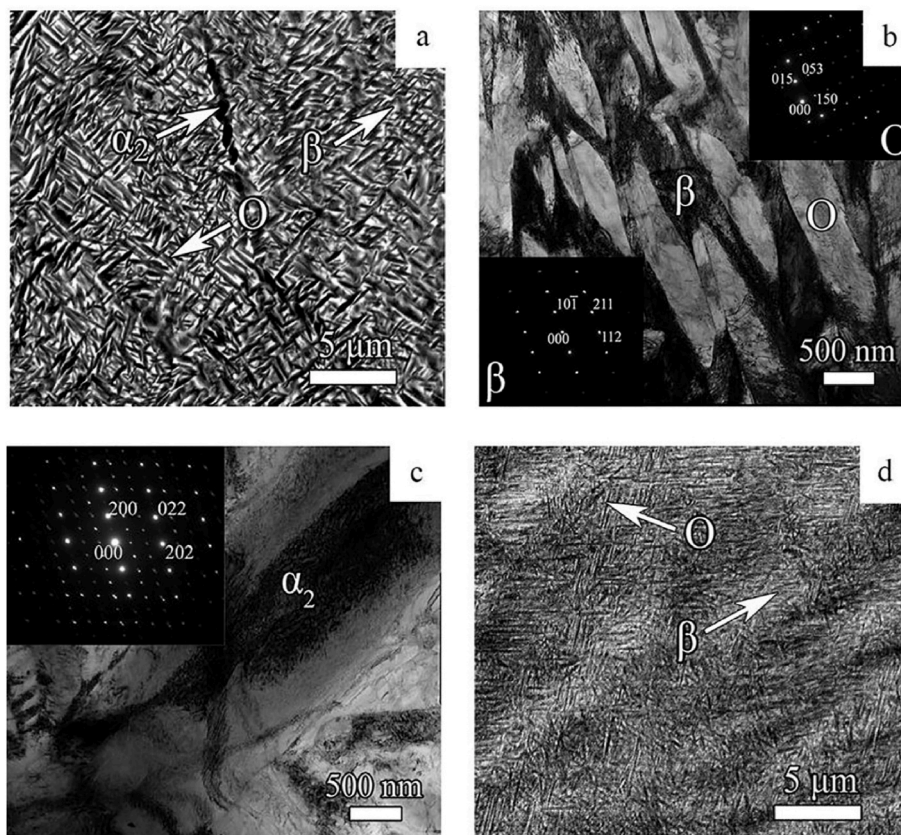

Fig. 13. Structure of FZ after LBW at 400 °C and subsequent heat treatment: (a), (d) - BSE-SEM images; (b), (c) - TEM images; (a), (b), (c) – microstructure after PWHT1; (d) - microstructure after PWHT2.
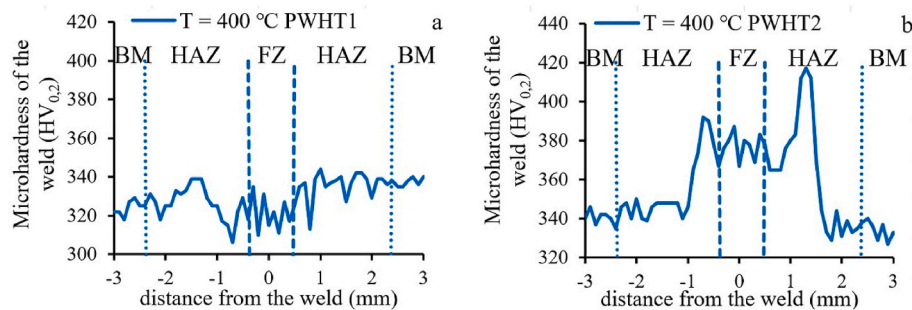
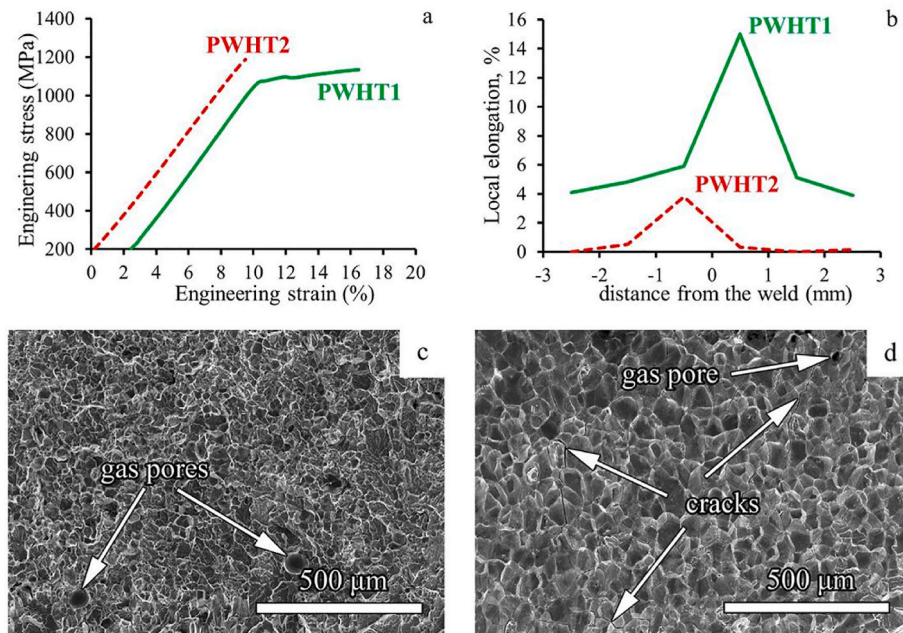**Fig. 14.** Microhardness distribution across welds with pre-heating at 400 °C after (a) PWHT1 and (b) PWHT2.

Fig. 15. (*a*) Stress-strain curves and (*b*) distribution of the local strain along the gauge length of tensile specimens after LBW at 400 °C and PWHT; SE - SEM images of the fracture surfaces of the tensile specimens after (*c*) PWHT1 and (*d*) PWHT2.

2. An attractive combination of strength and ductility was obtained in the LBWed-at-400 °C joints after air quenching from 920 °C with subsequent aging at 800 °C (PWHT1). In comparison with single aging at 800 °C (PWHT2), high ductility (TE = 6.5%) corresponded to a higher amount of the soft β-phase, coarser O-phase precipitates in the weld and expected release of residual stresses during holding at 920 °C. The lack of ductility after other LBW modes did not regain using applied post-weld heat treatment modes.

Author statement

Dmitrii Panov: investigation, methodology, visualization, writing-original draft preparation; Stanislav Naumov: investigation, methodology, visualization, writing-original draft preparation; Vitaliy Sokolovsky, Elena Volokitina, Elizaveta Povolyaeva: investigation, methodology; Nikolai Kashaev, Volker Ventzke, René Dinse, Stefan Riekehr: resources, methodology, writing-review and editing; Nadezda Nochovnaya, Evgeniy Alekseev: resources, methodology; Nikita Stepanov, Sergey Zherebtsov: validation, writing-review and editing; Gennady Salishchev: writing-review and editing, conceptualization.

Declaration of competing interest

The authors declare that they have no known competing financial interests or personal relationships that could have appeared to influence the work reported in this paper.

Appendix A. Supplementary data

Supplementary data to this article can be found online at https://doi.org/10.1016/j.intermet.2022.107466.

References

[1] J. Kumpfert, Intermetallic alloys based on orthorhombic titanium aluminide, Adv. Eng. Mater. 3 (2001) 851–864, https://doi.org/10.1002/1527-2648(200111)3:11<851:AID-ADEM851>3.0.CO;2-G.
[2] W. Chen, J.W. Li, L. Xu, B. Lu, Development of Ti2AlNb alloys: opportunities and challenges, Adv. Mater. Process. 172 (5) (2014) 23–27.
[3] X.Q. Cai, Y. Wang, Z.W. Yang, D.P. Wang, Y.C. Liu, Transient liquid phase (TLP) bonding of Ti2AlNb alloy using Ti/Ni interlayer: microstructure characterization

and mechanical properties, J. Alloys Compd. 679 (2016) 9–17, https://doi.org/10.1016/j.jallcom.2016.03.286.

[4] X. Li, G. Wang, Y. Gu, D. Li, H. Fang, Investigation on electrically-assisted diffusion bonding of Ti2AlNb alloy sheet by microstructural observation, mechanical tests and heat treatment, Mater. Des. 157 (2018) 351–361, https://doi.org/10.1016/j.matdes.2018.07.049.

[5] X. Liu, S. Wu, Y. Ji, L. Shao, H. Zhao, X. Wan, Ultrasonic frequency pulse tungsten inert gas welding of Ti2AlNb-based alloy, Xiyou Jinshu/Chinese J. Rare Met. 38 (2014) 541–547, https://doi.org/10.13373/j.cnki.cjrm.2014.04.001.

[6] D. Cai, J. Chen, X. Mao, C. Hao, Reheat cracking in Ti2AlNb alloy resistance spot weldments, Intermetallics 38 (2013) 63–69, https://doi.org/10.1016/j.intermet.2013.02.013.

[7] Y. jun Li, A. ping Wu, Q. Li, Y. Zhao, R. can Zhu, G. qing Wang, Effects of welding parameters on weld shape and residual stresses in electron beam welded Ti 2 AlNb alloy joints, Trans. Nonferrous Met. Soc. China English Ed. 29 (2019) 67–76, https://doi.org/10.1016/S1003-6326(18)64916-7.

[8] X. Chen, F.Q. Xie, T.J. Ma, W.Y. Li, X.Q. Wu, Effects of post-weld heat treatment on microstructure and mechanical properties of linear friction welded Ti2AlNb alloy, Mater. Des. 94 (2016) 45–53, https://doi.org/10.1016/j.matdes.2016.01.017.

[9] D. Li, S. Hu, J. Shen, H. Zhang, X. Bu, Microstructure and mechanical properties of laser-welded joints of Ti-22Al-25Nb/TA15 dissimilar titanium alloys, J. Mater. Eng. Perform. 25 (2016) 1880–1888, https://doi.org/10.1007/s11665-016-2025-4.

[10] J. Zou, H. Li, Review on weldability of Ti2AlNb-based alloy, Mater. China. 38 (2019) 710–716, https://doi.org/10.7502/j.issn.1674-3962.201803012.

[11] Z. Lei, H. Zhou, Y. Chen, K. Zhang, B. Li, A comparative study of deformation behaviors between laser-welded joints and base metal of Ti-22Al-24.5Nb-0.5Mo alloy, J. Mater. Eng. Perform. 28 (2019) 5009–5020, https://doi.org/10.1007/s11665-019-04224-7.

[12] Z. Lei, K. Zhang, H. Zhou, L. Ni, Y. Chen, A comparative study of microstructure and tensile properties of Ti2AlNb joints prepared by laser welding and laser-additive welding with the addition of filler powder, J. Mater. Process. Technol. 255 (2018) 477–487, https://doi.org/10.1016/j.jmatprotec.2017.12.044.

[13] B. Sarre, S. Flouriot, G. Geandier, B. Panicaud, V. De Rancourt, Mechanical behavior and fracture mechanisms of titanium alloy welded joints made by pulsed laser beam welding, Procedia Struct. Integr. 2 (2016) 3569–3576, https://doi.org/10.1016/j.prostr.2016.06.445.

[14] J. Wu, L. Xu, Z. Lu, B. Lu, Y. Cui, R. Yang, Microstructure design and heat response of powder metallurgy Ti2AlNb alloys, J. Mater. Sci. Technol. 31 (2015) 1251–1257, https://doi.org/10.1016/j.jmst.2015.09.006.

[15] K. Muraleedharan, A.K. Gogia, T.K. Nandy, D. Banerjee, S. Lele, Transformations in a Ti-24Al-15Nb alloy: Part I. Phase equilibria and microstructure, Metall. Trans. A 23 (1992) 401–415, https://doi.org/10.1007/BF02801158.

[16] Y. Wu, G. Liu, Z.Q. Liu, Z.J. Tang, B. Wang, Microstructure, mechanical properties and post-weld heat treatments of dissimilar laser-welded Ti2AlNb/Ti60 sheet, Rare Met. (2018) 1–11, https://doi.org/10.1007/s12598-018-1047-5.

[17] X.H. Zhao, Y.T. Liu, C. Ye, Y.Z. Zhang, Effects of heat treatment on microstructure and microhardness of laser melting deposited Ti-22Al-25Nb alloy, Mater. Res. Innovat. 19 (2015) 823–830, https://doi.org/10.1179/1432891715Z.0000000001813.

[18] R. Patterson, P. Martin, B. Damkroger, L. Christodoulou, Titanium aluminide: electron beam weldability, Weld. J. 69 (1990) 39–44.

[19] E. Panina, N. Yurchenko, S. Zherebtsov, N. Stepanov, G. Salishchev, V. Ventzke, R. Dinse, N. Kashaev, Laser beam welding of a low density refractory high entropy alloy, Metals 9 (2019), https://doi.org/10.3390/met9121351.

[20] I. Polozov, V. Sufiiarov, A. Kantyukov, I. Razumov, I. Goncharov, T. Makhmutov, A. Silin, A. Kim, K. Starikov, A. Shamshurin, A. Popovich, Microstructure, densification, and mechanical properties of titanium intermetallic alloy manufactured by laser powder bed fusion additive manufacturing with high-temperature preheating using gas atomized and mechanically alloyed plasma spheroidized powder, Addit. Manuf. 34 (2020), https://doi.org/10.1016/j.addma.2020.101374.

[21] K. Zhang, Z. Lei, Y. Chen, K. Yang, Y. Bao, Heat treatment of laser-additive welded Ti2AlNb joints: microstructure and tensile properties, Mater. Sci. Eng. 744 (2019) 436–444, https://doi.org/10.1016/j.msea.2018.12.058.

[22] Y.B. Alexeev, N.A. Nochovnaya, V.I. Ivanov, P.V. Panin, A.V. Novak, Investigation of the effect of aluminium content on phase composition and thermomechanical mode of isothermal forging of VTI-4 intermetallic alloy, Light Alloy Technol 1 (2015) 57–61.

[23] I. Burkhardt, V. Ventzke, S. Riekehr, N. Kashaev, J. Enz, Laser welding and microstructural characterization of dissimilar γ-TiAl-Ti6242 joints, Intermetallics 104 (2019) 74–83, https://doi.org/10.1016/j.intermet.2018.09.012.

[24] Y. Zheng, W. Zeng, D. Li, J. Xu, X. Ma, X. Liang, J. Zhang, Orthorhombic precipitate variant selection in a Ti2AlNb based alloy, Mater. Des. 158 (2018) 46–61, https://doi.org/10.1016/j.matdes.2018.08.011.

[25] N. Kashaev, D. Pugachev, V. Ventzke, F. Fomin, I. Burkhardt, J. Enz, S. Riekehr, Microstructure and mechanical performance of autogenously fibre laser beam welded Ti-6242 butt joints, Mater. Sci. Eng. 694 (2017) 110–120, https://doi.org/10.1016/j.msea.2017.03.115.

[26] K. Zhang, L. Ni, Z. Lei, Y. Chen, X. Hu, Microstructure and tensile properties of laser welded dissimilar Ti-22Al-27Nb and TA15 joints, Int. J. Adv. Manuf. Technol. 87 (2016) 1685–1692, https://doi.org/10.1007/s00170-016-8579-3.

[27] L. Wang, D. Sun, H. Li, X. Gu, C. Shen, Microstructures and mechanical properties of a laser-welded joint of Ti3Al-Nb alloy using pure Nb filler metal, Metals 8 (2018), https://doi.org/10.3390/met8100785.

[28] J. Małecka, Investigation of the oxidation behavior of orthorhombic Ti2AlNb alloy, J. Mater. Eng. Perform. 24 (2015) 1834–1840, https://doi.org/10.1007/s11665-015-1449-6.

[29] P.S. Liu, W.A. Baeslack, J. Hurley, Dissimilar alloy laser beam welding of titanium, Ti-6Al-4V to beta-C, Weld. J. (Miami, Fla) (1994) 175–181.

[30] K. Zhang, M. Liu, Z. Lei, Y. Chen, Microstructure evolution and tensile properties of laser-TIG hybrid welds of Ti2AlNb-based titanium aluminide, J. Mater. Eng. Perform. 23 (2014) 3778–3785, https://doi.org/10.1007/s11665-014-1153-y.

[31] H. B, Z.W. Xiaohong Zhan, Tingyan Yan, Qiyu Gao, Zhenxin Zhu, The porosity formation mechanism in the laser welded joint of TA15 titanium alloy, Mater. Res. Express 27 (2019) 0–31, https://doi.org/10.1088/2053-1591/ab1612.

[32] I. Polozov, V. Sufiiarov, A. Kantyukov, A. Popovich, Selective Laser Melting of Ti2AlNb-based intermetallic alloy using elemental powders: effect of process parameters and post-treatment on microstructure, composition, and properties, Intermetallics 112 (2019), https://doi.org/10.1016/j.intermet.2019.106554.

[33] F.C. Dary, T.M. Pollock, Effects of high temperature air and vacuum exposures on the room temperature tensile behavior of the (O + B2) titanium aluminide Ti-22Al-23Nb, Mater. Sci. Eng. 208 (1996) 188–202, https://doi.org/10.1016/0921-5093(95)10049-0.

[34] M. Yan, W. Xu, M.S. Dargusch, H.P. Tang, M. Brandt, M. Qian, Review of effect of oxygen on room temperature ductility of titanium and titanium alloys, Powder Metall. 57 (2014) 251–257, https://doi.org/10.1179/1743290114Y.0000000108.

[35] M.T. Jia, D.L. Zhang, B. Gabbitas, J.M. Liang, C. Kong, A novel Ti-6Al-4V alloy microstructure with very high strength and good ductility, Scripta Mater. 107 (2015) 10–13, https://doi.org/10.1016/j.scriptamat.2015.05.008.

[36] Y.N. Saraev, I.M. Poletika, A.V. Kozlov, E.G. Khomchenko, Formation of structure and properties of welds input during pulse welding, Phys. Mesomech. 8 (2005) 137–140.

[37] J. Wu, L. Xu, Z. Lu, Y. Cui, R. Yang, Preparation of powder metallurgy Ti-22Al-24Nb-0.5Mo alloys and electron beam welding, Jinshu Xuebao/Acta Metall. Sin. 52 (2016) 1070–1078, https://doi.org/10.11900/0412.1961.2016.00019.